Supplementary Methods

Sample fabrication

The substrate is composed of a 100nm thick low-stress SiN layer on top of a Si wafer. The Cooper-Pair Box (CPB) is patterned using electron-beam lithography and double-angle evaporation of aluminum.[31] The thickness of the island and the ground leads are ~ 60 nm and ~ 20 nm respectively. The island is coupled to the ground leads via two small (~ 100 x 100 nm^2) Al/AlO_x/Al Josephson tunnel junctions, and is arranged in a DC-SQUID configuration.

The aluminum layer used to define the nanoresonator, and which ultimately serves as the electrode on top of the nanoresonator, is patterned in the same step as the CPB. This layer acts as an etch mask for undercutting the nanoresonator. To protect the CPB during etching, a layer of PMMA is spun on the sample, and a small window defining the nanoresonator is opened using a second e-beam lithography step. The nanoresonator is then undercut in an ECR etcher with Ar/NF3 plasma: The first step is an anisotropic SiN etch that defines the resonator beam; and the second is an isotropic etch of the underlying Si to undercut the beam.

Sample characteristics

$\omega_{NR}/(2\pi) = 58$ MHz	Nanoresonator fundamental in-plane resonance frequency.
$K \sim 60\,\mathrm{N/m}$	Nanoresonator effective spring constant given by $K = \alpha M_{geom}\omega_{NR}^2$, where $M_{geom} \approx 9\times10^{-16}kg$ is the estimated geometrical mass and α=.48 is found by assuming that the CPB couples to the average displacement of the nanoresonator over the length of the CPB island.
$Q \approx$ 30,000-60,000	Typical nanoresonator quality factor for the range of T_{mc}, V_{GNR}, and V_{NR} used.
$E_C/h \approx 13-15$ GHz	Estimated CPB charging energy from spectroscopy (lower bound) and LZ measurements (upper bound).
$E_{J0}/h \approx 13$ GHz	Estimated CPB maximum Josephson energy from spectroscopy.
$C_{NR} = 43$ aF	Measured nanoresonator-to-CPB capacitance.
$d \sim 300$ nm	Resonator/CPB spacing.

$\partial C_{NR}/\partial x \sim 40-50$ pF/m	Derivative of nanoresonator/CPB capacitance estimated from FEMLAB.
$C_{cpb} = 17$ aF	Measured CPB gate capacitance.
$\lvert\lambda/(2\pi)\rvert \sim .3-2.3$ MHz	Coupling strength calculated using Eq.1 and the parameters $E_C/h = 14$ GHz, $K = 60$ N/m, $\frac{\partial C_{NR}}{\partial x} = 50$ pF/m, and $V_{NR} = 2-15$ V.
$\lvert\lambda/(2\pi)\rvert \sim .5-3$ MHz	Coupling strength calculated using Eq. 3 and $\Delta\omega_{NR}/(2\pi)$ data displayed in the inset of Fig. 1c, assuming CPB biased at charge degeneracy and $E_J/h = 12$ GHz.

Circuit and measurement description

The measurement set-up is shown in Fig.S1. We use capacitive displacement transduction and radio frequency reflectometry to measure the nanomechanical frequency shift $\Delta\omega_{NR}/(2\pi)$.[32] A DC potential difference $\Delta V = V_{GNR} - V_{NR}$ is applied across the capacitor C_{GNR}, coupling the nanoresonator's motion to the charge on the actuation-detection electrode. Upon application of $V_{RF}(\omega)$ to the electrode, the response of the coupled nanoresonator-electrode system can be modeled as a series RLC circuit with impedance

$Z_{NR}(\omega) = jL_{NR}\left(\omega^2 - \omega_{NR}^2\right)/\omega + R_{NR}$.[32] Here $R_{NR} \approx Kd_{GNR}^2/(\omega_{NR} Q \alpha_{GNR}^2 C_{GNR}^2 \Delta V^2)$ and $L_{NR} = QR_{NR}/\omega_{NR}$, where $d_{GNR} \sim 100\,nm$ is the spacing between the nanoresonator and electrode and α_{GNR} is a geometric coefficient of order unity. For typical values of coupling voltage used in our experiment, $\Delta V \sim 5-10$ V, $R_{NR} \sim .5-2\ M\Omega >> Z_0$, where $Z_0 = 40\,\Omega$ is the characteristic impedance of the transmission line feeding the actuation-detection electrode.

To overcome the impedance mismatch, we use an LC network to transform $Z_{NR}(\omega_{NR})$ closer to Z_0. The LC network is formed by a commercial, copper-wound coil (nominally L_T = 5.6 μH) and the stray capacitance (C_T ~ 1.0 pF) of the PC board upon which the sample sits. The components are chosen so that $\omega_{LC} = \sqrt{1/(L_T C_T)} \approx \omega_{NR}$. Thus when the RF drive frequency is tuned into resonance with the nanoresonator and LC circuit, $\omega = \omega_{NR} = \omega_{LC}$, the total impedance seen looking from the transmission line into the impedance matching network is given by $Z(\omega_{NR}) = L_T/(C_T R_{NR})$, where it is assumed for simplicity that the matching network is lossless. For our parameters, we estimate that we achieve $Z(\omega_{NR}) \sim 2-10\,\Omega$.

For perfect matching to the transmission line, $Z(\omega_{NR}) = Z_0$, the reflection coefficient $\Gamma = (Z(\omega_{NR}) - Z_0)/(Z(\omega_{NR}) + Z_0) = 0$. However, a small change in the nanoresonator's frequency $\Delta\omega_{NR}/(2\pi)$ leads to a correction given by $\Delta\Gamma \approx jQ\Delta\omega_{NR}/\omega_{NR}$. Thus a shift in the nanomechanical frequency $\Delta\omega_{NR}/(2\pi)$ can be monitored by tracking the shift $\Delta V_r = \Delta\Gamma V_{RF}$

in the reflected component of the RF drive signal. This is accomplished by embedding the nanoresonator in a phase-lock loop (Fig. S2). Essentially, a directional coupler routes the reflected signal to a phase-sensitive detector, the output of which is fed into a VCO that supplies $V_{RF}(\omega)$.

The measurement is done on a dilution refrigerator located inside of a RF-shielded room. Four DC lines are used: V_{cpb} for biasing the CPB; V_{NR} for controlling the coupling between the CPB and nanoresonator; V_{GNR} for controlling the coupling between the nanoresonator and detection circuit; and V_{flux} (not shown) for biasing a homemade current source to energize the solenoid for application of flux Φ to the CPB. V_{cpb} and V_{flux} are supplied by a DAC card and routed into the shielded room using optical isolators. V_{NR} and V_{GNR} are supplied by batteries located in the shielded room. V_{cpb}, V_{NR}, and V_{GNR} are filtered at room temperature (RT) at the input to the dilution refrigerator using commercial Pi-filters and Cu powder filters.[33] From RT to the mixing chamber (MC), these lines are each composed of ~ 2 meters of lossy stainless steel coax, with two stages of Cu powder filters (at 1K and MC). The typical total attenuation from RT to MC is measured to be ~-100 dB at 10 GHz.

High frequency lines providing radio frequency excitation V_{RF} of the nanoresonator and microwave excitation V_{μ} of the CPB are routed into the shielded room through DC blocks

and into the dilution refrigerator via commercial high-pass filters and attenuators. They are attenuated and thermalized at 1 K using cryogenic-compatible attenuators. At 1K, V_{RF} is fed into the coupled port (-20 dB) of a directional coupler for the reflectometry measurements: The Output port of the directional coupler feeds V_{RF} to the actuation gate electrode of the nanoresonator for excitation; And the Input port of the directional coupler feeds the reflected component V_r through a Miteq AFS-series cryogenic amplifier to the room temperature electronics that compose the phase-lock loop (Fig. S2). Bias-tees anchored to the MC are used to combine V_μ and V_{RF} with V_{cpb} and V_{GNR} respectively. To provide additional filtering between the MC and sample stage, all lines are fed through lossy stainless steel coax.

Supplementary Discussion

Model of dispersive shift incorporating the full CPB Hamiltonian

The spin-1/2 approximation for the CPB Hamiltonian is only appropriate in the vicinity of a charge degeneracy point. Thus to model the dispersive frequency shift $\Delta\omega_{NR}/(2\pi)$ of the nanoresonator over the full range of gate voltages V_{cpb} used in the experiment (e.g. Fig. 2b) we employ the full expressions for the CPB[34] and interaction Hamiltonians, given respectively by

$$\hat{H}_{CPB} = \sum_n \left\{ 4E_C \left(n - n_{cpb} - n_{NR}\right)^2 |n\rangle\langle n| - \frac{E_J}{2}\left(|n+1\rangle\langle n| + |n\rangle\langle n+1|\right)\right\} \quad \text{(S1)}$$

and

$$\hat{H}_{\text{int}} = -\sum_{n} 2\lambda\hbar\left(n - n_{cpb} - n_{NR}\right)\left(\hat{a} + \hat{a}^{\dagger}\right)\cdot\left|n\right\rangle\left\langle n\right| \qquad \text{(S2)}.$$

To account for contributions from charge states other than n and $n+1$, 11 adjacent charge states are included in the model. Using Matlab, we first calculate numerically the eigenstates of the uncoupled Hamiltonian $\hat{H} = \hat{H}_{CPB} + \hat{H}_{NR}$ as a function of a V_{cpb} and Φ, where $\hat{H}_{NR}$ remains as defined in the main text. The correction to the energy levels due to $\hat{H}_{\text{int}}$ and hence the dispersive shift of the nanoresonator $\Delta\omega_{NR}/(2\pi)$ are then calculated using second-order time-independent perturbation theory. It is important to note, that in the vicinity of a charge degeneracy point, $.25 \le n_{CPB} \le .75$, use of the full CPB Hamiltonian results in < 5% correction to $\Delta\omega_{NR}/(2\pi)$ calculated from Eq. 3 (at degeneracy the correction is $\lesssim$ 1%).

Periodicity of dispersive shift in V_{cpb} and Φ

Figure S3a displays the 2e-to-e transition in periodicity of nanoresonator's frequency shift $\Delta\omega_{NR}/(2\pi)$ with respect to V_{cpb}, taken with flux biased so that $E_J \sim E_{J0}$. At a mixing chamber temperature of 120 mK, the periodicity is primarily 2e-periodic with peaks spaced by $\Delta V_{cpb} = 18.7$ mV, corresponding to a gate capacitance $C_g = 17.1$ aF. At temperatures of 40 mK and below, the quasiparticle poisoning rates greatly exceed the measurement time, and periodicity is primarily e-periodic with peaks spaced by $\Delta V_{cpb} \approx 9 - 10$ mV.

Figure S3b displays the periodicity in applied flux Φ of $\Delta\omega_{NR}/(2\pi)$ taken at a charge degeneracy point. The average spacing between the peaks is found to be $\Delta B \sim 200\,\mu\mathrm{T}$. While there is large uncertainty in the effective area of the split-junction CPB, we can estimate the flux periodicity using the geometric area of the CPB loop $A \sim 5\ \mu m^2$. This yields a flux periodicity of $\Delta\Phi \sim 1 \times 10^{-15}$ T-m^2 in reasonable agreement with the expected periodicity of one flux quantum $\Phi_o = 2.07 \times 10^{-15}$ T m^2. The background increase in ω_{NR} during the course of the measurement was not typical of most magnetic field sweeps, which were taken over a much smaller range.

The x-axes of Figure 2a (main text) and Figures 3a-d (main text) were converted into units of the flux quantum Φ_o by assuming that, at charge degeneracy, adjacent minima in $\Delta\omega_{NR}/(2\pi)$ were separated in flux by Φ_o. For the data in Figure 2 (main text), the magnetic field sweep was applied on top of a static field of ~ 0.01 T. For the data in Figure 3 (main text), the magnetic field sweep was applied on top of a static field of ~ 0.015 T.

Charge-drift correction

For a typical $\Delta\omega_{NR}/(2\pi)$ vs. V_{cpb} vs. Φ "map" measurement, the flux Φ was held constant while we swept V_{cpb} and recorded $\Delta\omega_{NR}/(2\pi)$. The flux was then incremented, and the process repeated. For each constant flux trace, we typically averaged for ~ sec's. Since the

effective gate charge had a slow drift component, a post-processing correction method was employed in order to erase the drift and to average multiple maps taken over long periods of time. Figure S4a is the uncorrected $\Delta\omega_{NR}/(2\pi)$ vs. V_{cpb} vs. Φ map for Figure 2a (main text). In this instance, we chose two charge periods in the map and fit $\Delta\omega_{NR}/(2\pi)$ vs. V_{cpb} to two Gaussian peaks for each value of flux Φ. A typical trace and fit, taken at Φ =-0.45 (A.U.), is displayed in Fig. S4b. The fit gave us the positions of the charge degeneracy points and allowed us to align traces taken at successive values of Φ as well as subtract offsets due to background fluctuations in $\omega_{NR}/(2\pi)$, typically on the order of 10's Hz. Figure 2a (main text) is the result of only one such post-processed map.

For the spectroscopy maps in Figs.3a-d (main text) and the Landau-Zener map in Fig. 4a (main text), as many as 14 maps were taken over the course of a day. Because the presence of the microwave resonances in these maps made it difficult to fit and find the location of the charge degeneracy points, it was essential, for each value of Φ, to take one trace with microwaves applied and then a second trace immediately afterward without microwaves applied. This allowed us to use the maps without microwaves applied to correct the charge drift of the maps with microwaves applied. For better precision, a second post-processing step was used that minimized the variance at each value of Φ between traces of different maps. For reference, one of the five 'uncorrected' Landau-Zener maps taken at

$\omega_\mu/(2\pi) = 6.50$ GHz that were averaged together to produce Fig. 4a (main text) is displayed in Figure S5.

Determination of qubit parameters E_C and E_{J0} from spectroscopy

We can estimate the charging energy E_C and Josephson energy E_J of the qubit from spectroscopy by plotting, for fixed E_J, $\omega_\mu/(2\pi)$ versus the displacement from degeneracy Δn_{cpb} at which resonance occurs (i.e. $\Delta E = \hbar\omega_\mu$). Figure S6 displays $\omega_\mu/(2\pi)$ vs. Δn_{cpb} for several values of Φ. From the fits to $\omega_\mu/(2\pi) = \sqrt{(8E_c\Delta n_{cpb})^2 + (E_J)^2}/h$, we find $E_c/h = 13.7 \pm .4$ GHz, $E_c/h = 12.7 \pm .8$ GHz, $E_c/h = 13.4 \pm .2$ GHz for Φ =.1Φ_o, .2Φ_o and .35Φ_o respectively (all uncertainties are s.e.m.). From the intercepts of the fits, we find $E_J/h = 10.4 \pm .5$ GHz, $E_J/h = 9.5 \pm .9$ GHz, $E_J \approx 0$ GHz (large uncertainty) for Φ=.1Φ_o, .2Φ_o, and .35Φ_o respectively (all uncertainties are s.e.m.). The values of maximum Josephson energy E_{J0} inferred from the fits and the Josephson relation are ~10-15% smaller than what one would expect from the resonance condition $\hbar\omega_\mu = \Delta E = E_{J0}$, which occurs when $n_{cpb} = .5$ and $\Phi = 0$ (Fig. S7b). Comparing Fig. S7a and Fig. S7b, it is apparent that this occurs for microwave frequencies in the range of $\omega_\mu/(2\pi) = 12.5 - 13.5$ GHz, and thus we estimate $E_{J0}/h \sim 13$ GHz.

Figure S7 also serves to demonstrate the additional resonance features that appear near

charge degeneracy. The green-dashed lines denote the resonance bands we expect for the applied microwave frequency $\omega_\mu/(2\pi)$ based upon a calculation of ΔE from the full Hamiltonian Eq. S1. At the lowest microwave frequencies (Figs. S7a-b), the observed (n_{CPB},Φ)-dependence of the microwave resonance appears to be consistent with the coupling of the CPB island to an incoherent charge fluctuator.[35] However, we observed no apparent dependence of the additional resonant features on thermal cycling or background electric and magnetic fields. Additionally, we find that upon increasing $\omega_\mu/(2\pi)$ (Fig S7c-d), qualitative agreement between the observed and expected (n_{CPB},Φ)-dependence improves. Furthermore, it is apparent that there are resonant features where $\Delta\omega_{NR}>0$ (e.g. Fig. 3a (main text), Fig. 3d (main text), and Fig. S7c).

Qubit linewidth versus microwave amplitude

Recording the mechanical frequency shift $\Delta\omega_{NR}/(2\pi)$ as a function of the microwave frequency $\omega_\mu/(2\pi)$ (Fig. S8) we can also extract the driven qubit linewidth $\gamma/(2\pi)=\sqrt{1+\Omega_d^2T_2T_1}/(\pi T_2)$ (S3). As expected from Ω_d and Eq. S3, we find that $\gamma/(2\pi)$ increases with V_μ (Inset Fig. S8). From a fit of $\gamma/(2\pi)$ vs. V_μ^2 to Eq. S3 we find $T_2\geq 2\,n\,\mathrm{sec}$ at charge degeneracy.

Contour plots for Landau-Zener interferogram

The contour lines overlaying the Landau-Zener interferogram in Fig. 4a (main text) denote locations in (V_{cpb}, V_μ)-space where the phase of the CPB wavefunction is a multiple of 2π, i.e. $\varphi = 2\pi m$, where m is an integer. These contours were generated via the same method used in Ref. [36], with $\varphi_{L,R} = \frac{1}{\hbar}\int_{t_0}^{t_2} dt\Delta E(n_{cpb}(t)) - 2\varphi_S$. For a given V_{cpb} and V_μ, "L" and "R" correspond to the phase φ_L developed while the CPB traverses points to the left of charge degeneracy (i.e. V_{cpb} < -3.66 mV) and the phase φ_R developed while the CPB traverses points to the right of charge degeneracy (i.e. V_{cpb} >-3.66 mV) respectively. The Stokes phase φ_s, is also as defined in Ref. [36]. The parameters used to generate the overlay were $E_C / h = 14.0$ GHz, $E_{J0} / h = 13.2$ GHz, $C_g = 17.1$ aF, and $\omega_\mu / (2\pi) = 6.5$ GHz. As well, a factor of 2.8 was used to convert n_μ into V_μ, corresponding to an attenuation of 43.5 dB. Transmission measurements of the microwave circuit made at room temperature using a network analyzer with a 50 Ω input impedance yield ~50-54 dB attenuation. This is in reasonable agreement with value extracted from the LZ interferogram considering that the CPB gate presents an effectively open-circuit termination to the microwave line during operation.

Supplementary Notes

References for supporting online material

31. Fulton, T.A. & Dolan, G.J. Observation of single-electron charging effects in small tunnel junctions. *Phys. Rev. Lett.* **59**, 109 (1987).

32. Truitt, P.A. et al. Efficient and sensitive capacitive readout of nanomechanical resonator arrays. *Nano Lett.* **7**, 120-126 (2007).

33. Martinis, J.M, Devoret, M.H.& Clarke, J. Experimental tests for the quantum behavior of a macroscopic degree of freedom: The phase difference across a Josephson junction. *Phys. Rev. B* **35**, 4682-4698 (1987).

34. Makhlin, Y., Schon, G., & Shnirman, A. Quantum-state engineering with Josephson junction devices. *Rev. Mod. Phys.* **73**, 357-400 (2001).

35. Schuster, D.I. *Circuit Quantum Electrodynamics*. Ph.D. Thesis, Yale University (2007).

36. Sillanpaa, M. et al. Continuous-time monitoring of Landau-Zener interference in a Cooper-pair box. *Phys. Rev. Lett.* **96**, 187002 (2006).

Supplementary Figures and Legends

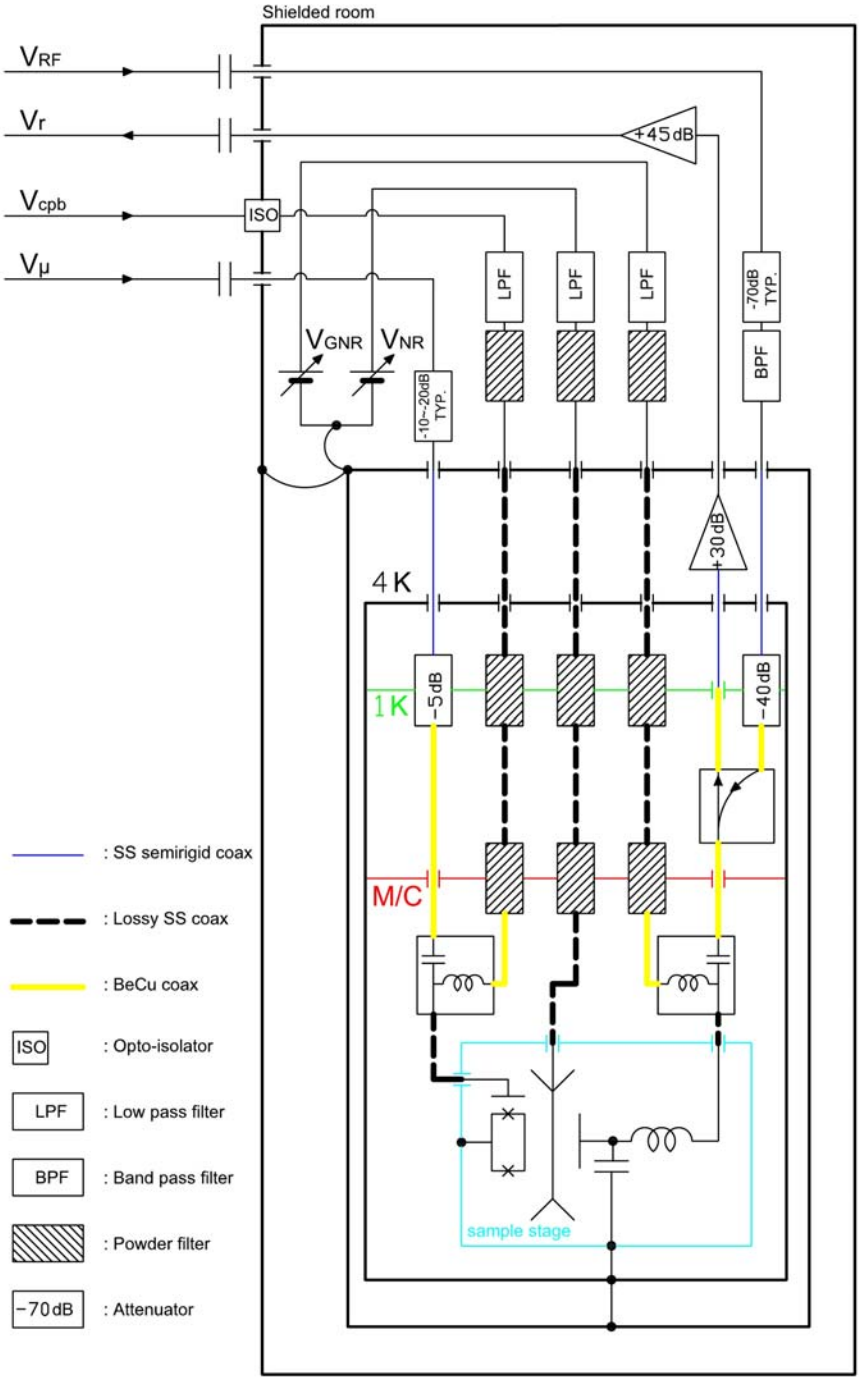

Figure S1: Schematic of measurement circuit

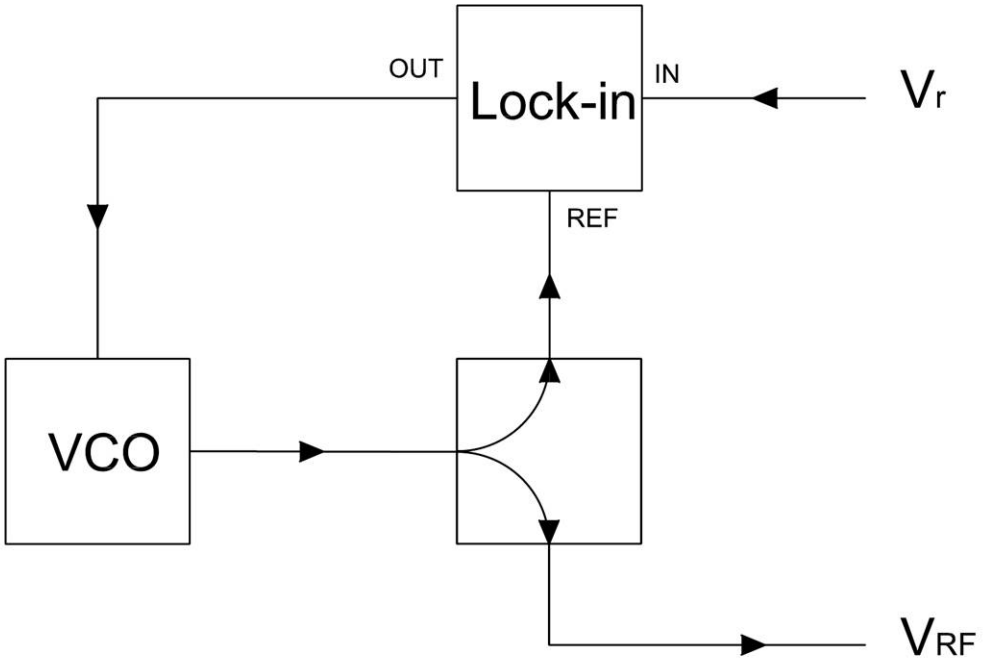

Figure S2. Phase-lock loop circuit. We use a phase-lock loop to measure the nanoresonator frequency shift $\Delta\omega_{NR}/(2\pi)$. The lock-in acts as a phase detector and low-pass filter which controls the voltage-controlled oscillator (VCO). The VCO output is split into two: One for exciting the nanoresonator V_{RF} and the other REF for the reference input of the lock-in.

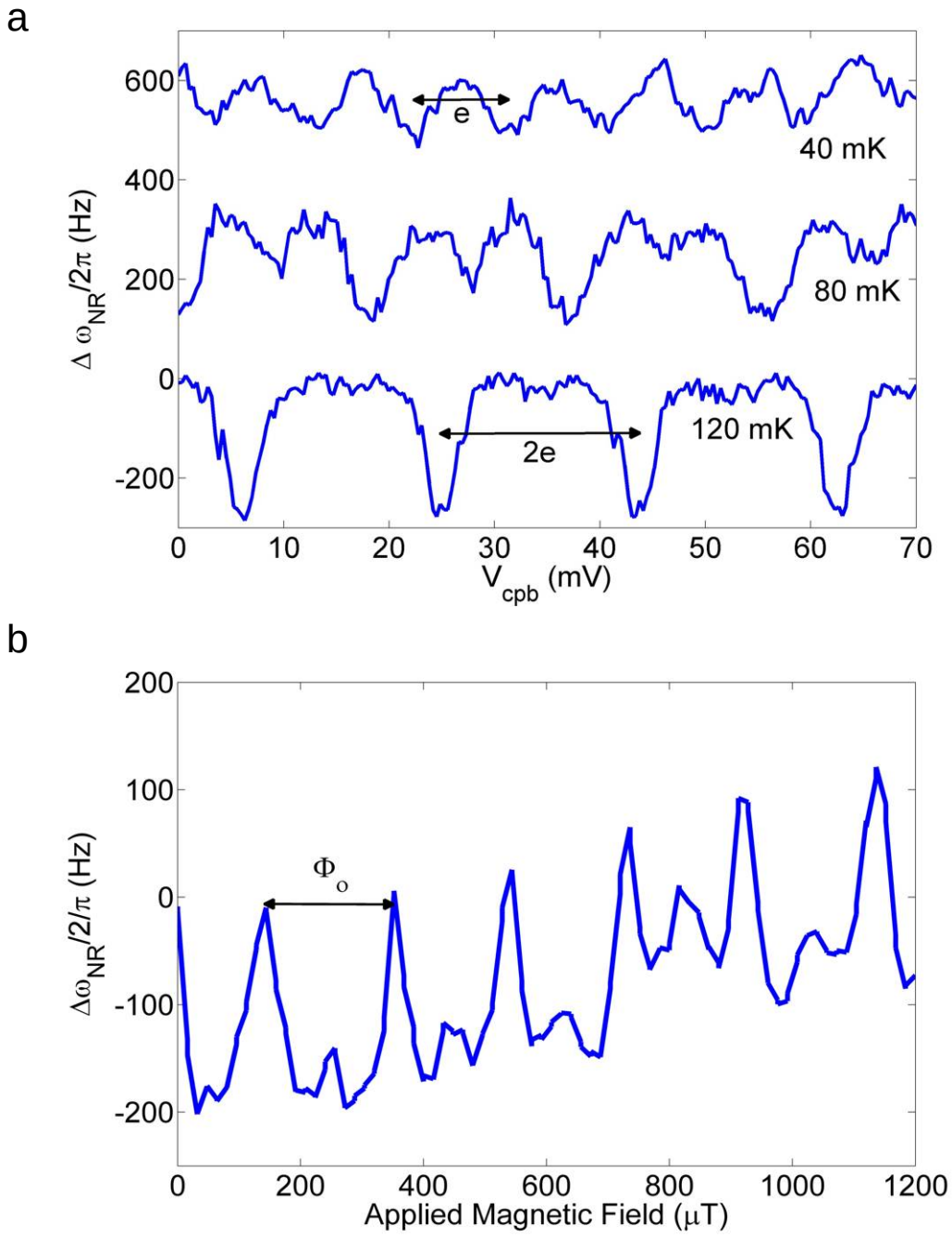

Figure S3. (a) 2*e*-*e* transition of the response in V_{cpb}. Data in (a) taken with $V_{NR} = 7$ V and flux bias set so that $E_J \sim E_{J0}$. (b) CPB flux periodicity. Data in (b) taken near a CPB charge degeneracy with $V_{NR} = 7$ V and $T_{mc} \sim 120$ mK.

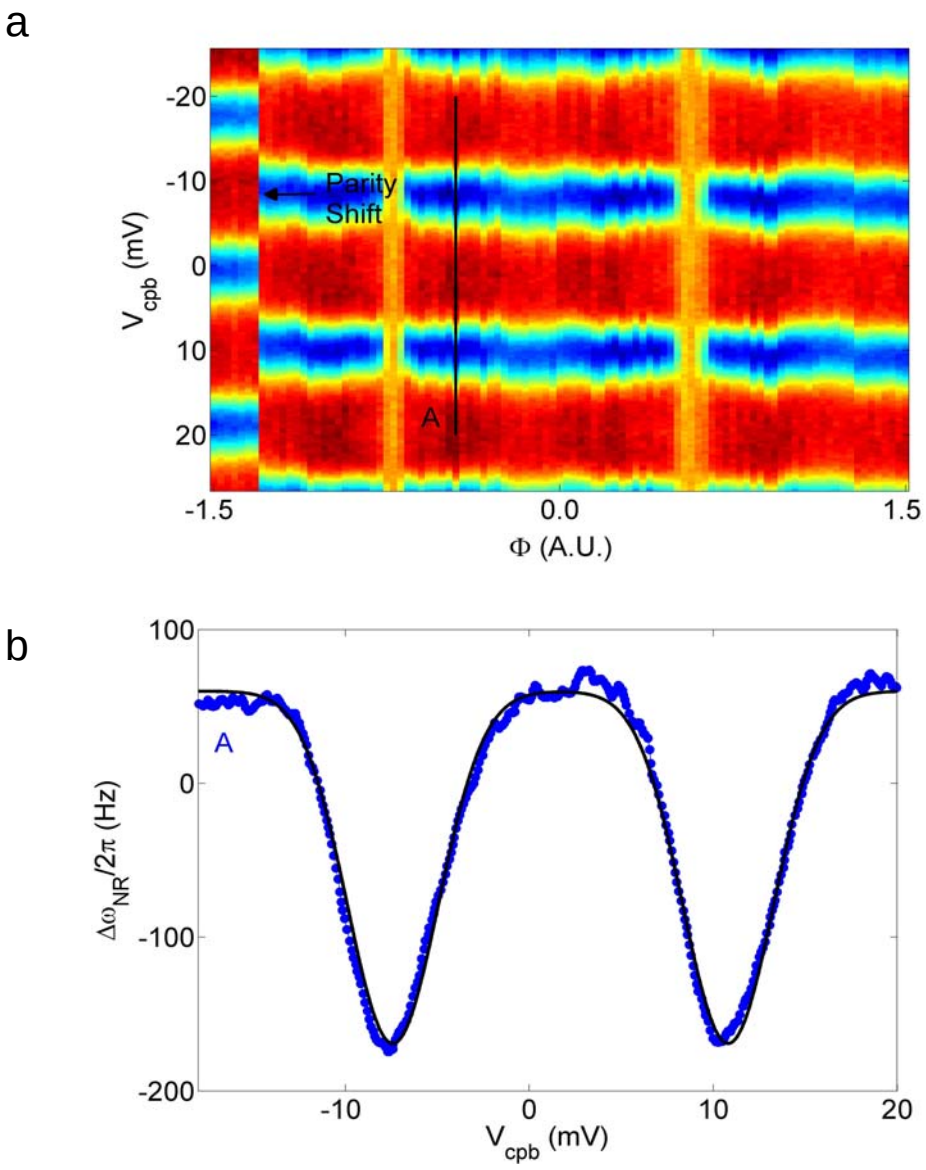

Figure S4: (a) Uncorrected data for Figure 2 (main text). A quasiparticle switching event is evident at Φ =-1.3. (b) Constant flux cross-section taken at "A", denoted by vertical black line in (a). Black line in (b) is a fit of the cross-section "A" to two Gaussian peaks to determine charge-offset and background change from trace-to-trace.

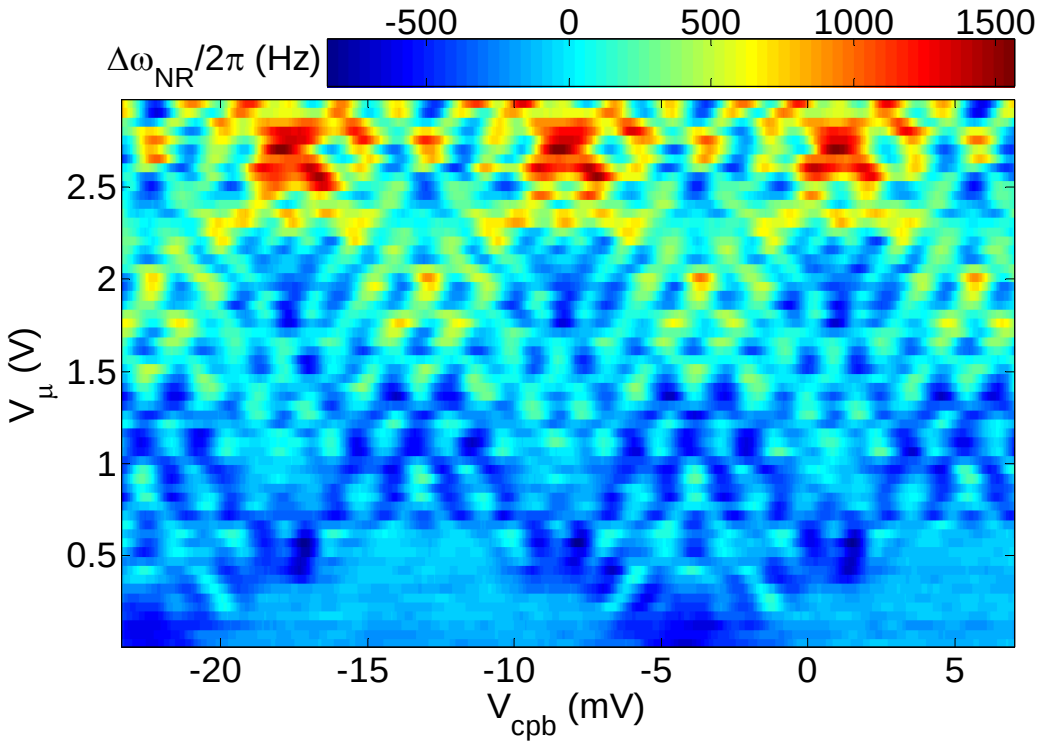

Figure S5: One map of $\Delta\omega_{NR}/(2\pi)$ vs. V_{cpb} vs. V_{μ} for $\omega_{\mu}/(2\pi) = 6.50$ GHz before charge drift is 'corrected'. This is one of five such maps; the average of the five maps is plotted in Fig.4a (main text).

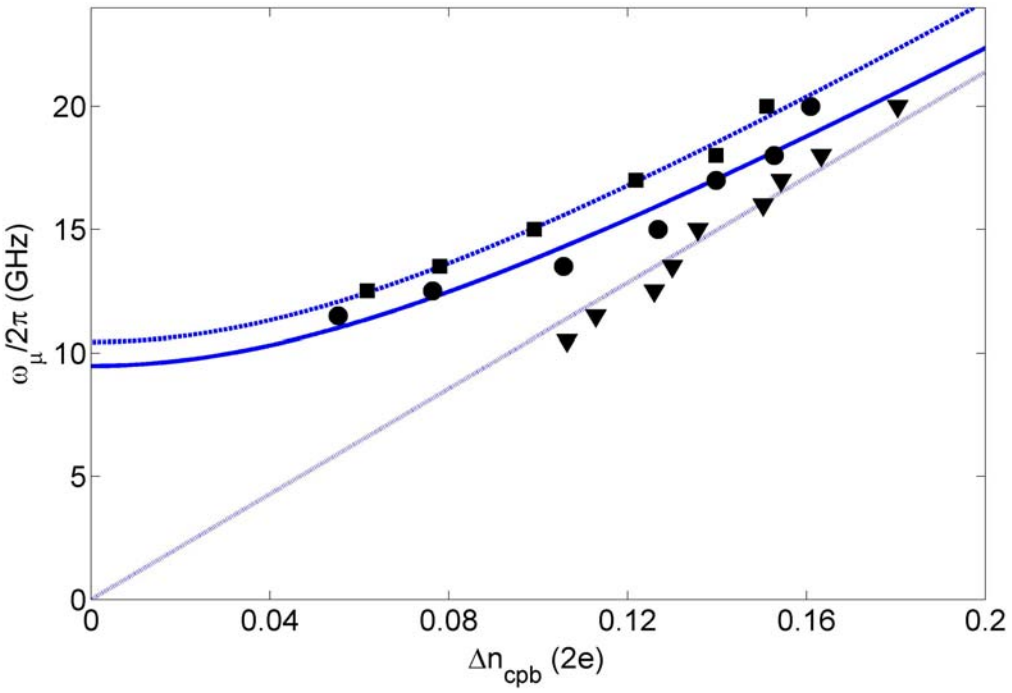

Figure S6: Plot of spectroscopic frequency $\omega_\mu/(2\pi)$ versus the value of Δn_{cpb} at which the CPB transition energy $\Delta E = \hbar\omega_\mu$, for Φ =.1Φ_o (squares), Φ =.2Φ_o (circles), Φ =.35Φ_o (triangles). Data is taken with $V_{NR} = 10$ V and $T_{mc} \sim 140$ mK.

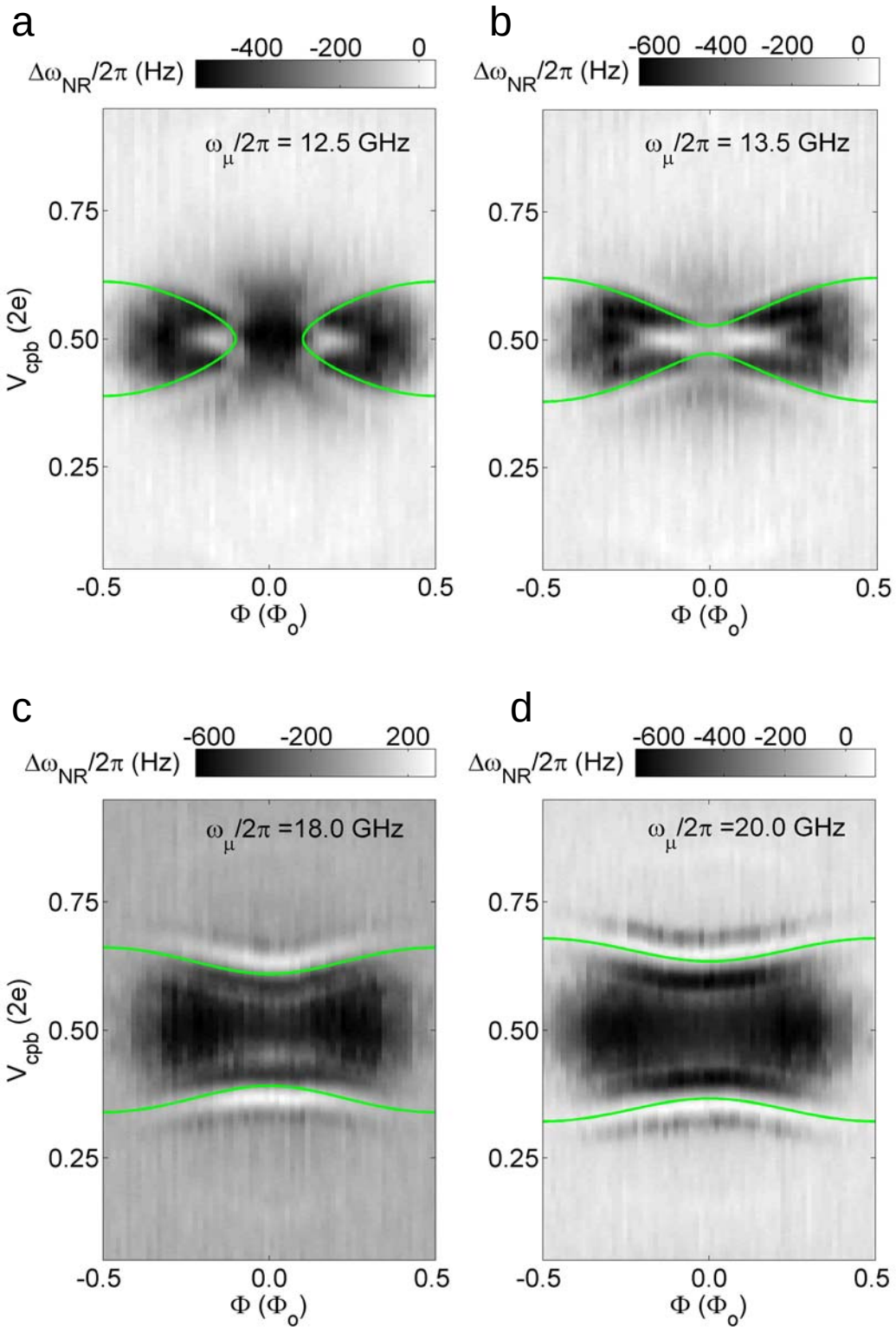

Figure S7: Measurements of the nanomechanical frequency shift $\Delta\omega_{NR}/(2\pi)$ versus

V_{cpb} and Φ for microwave frequencies (a) $\omega_\mu / (2\pi) = 12.5$ GHz (b) 13.5 GHz (c) 18 GHz (d) 20 GHz. Data taken at $V_{NR} = 10$ V and T_{mc} = 140 mK. The experimental values of V_{cpb} and Φ have been converted into units of Cooper pairs and the flux quantum Φ_o respectively. The maximum Josephson E_{J0} energy occurs at Φ / Φ_o = 0.0. When $\hbar\omega_\mu = E_{J0}$, the resonant hyperbola overlap at Φ / Φ_o = 0.0. Thus, from (a) and (b) we estimate that E_{j0}/h ~ 13 GHz. The green solid lines in the plots denote the expected resonance hyperbola determined from the qubit transition energy ΔE, which we calculate from the full CPB Hamiltonian Eq. S1 using $E_c / h = 14.0$ GHz and $E_{J0} / h = 13.2$ GHz.

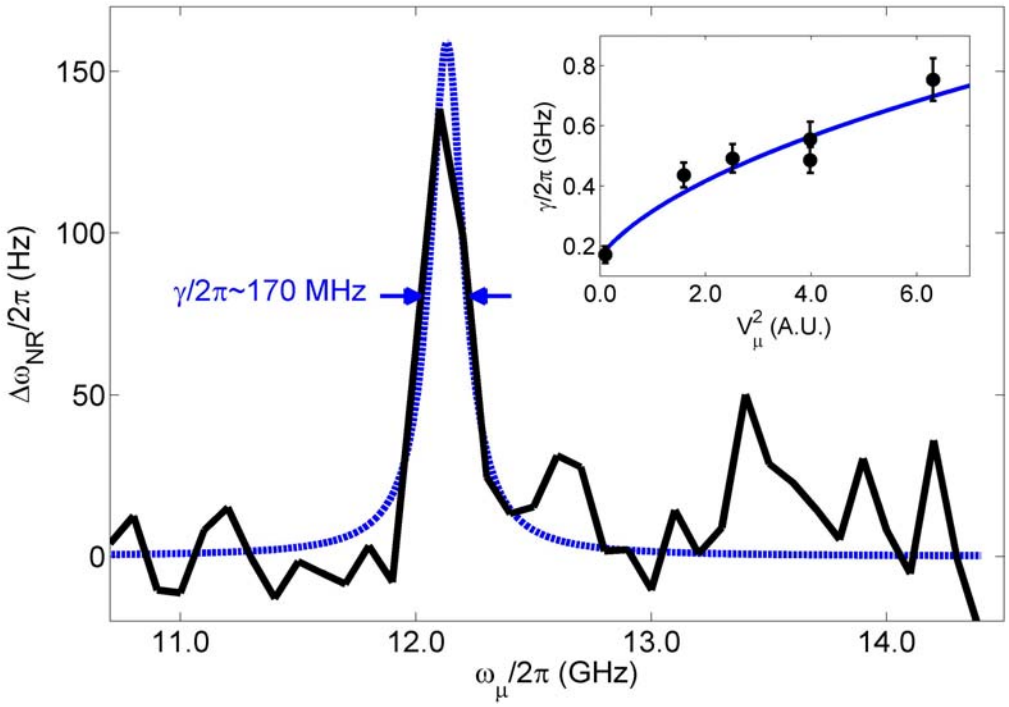

Figure S8. (Main) Nanoresonator frequency shift $\Delta\omega_{NR}/(2\pi)$ as a function of $\omega_\mu/(2\pi)$ at the smallest value of microwave amplitude V_μ used in the experiment. Data is taken with V_{cpb} biased near a charge degeneracy point, $V_{NR} = 8\,\mathrm{V}$, $T_{mc} \approx 100$ mK, and flux biased for $E_J/h \sim 12\,\mathrm{GHz}$. Background offset has been subtracted. The solid blue line is a fit to a Lorentzian. (Inset) The linewidth of the CPB transition plotted as a function of V_μ^2. Error bars are from a fit of each $\omega_\mu/(2\pi)$-sweep to a Lorentzian, and they denote the 68% confidence level (s.e.m). The solid-line is a fit to Eq. 4, demonstrating expected broadening of CPB transition due to increased microwave drive.